npj | climate and atmospheric science

www.nature.com/npjclimatsci

ARTICLE OPEN

Check for updates

A dynamic link between spring Arctic sea ice and the Tibetan Plateau snow increment indicator

Chao Zhang[1], Anmin Duan[1]✉, XiaoJing Jia[2], Zhibiao Wang[3] and Zhulei Pan[4,5]

Tibetan Plateau snow has long been recognized as a sensitive indicator of climate variability. However, the commonly used snow indicator cannot fully represent the interannual variability in late autumn Tibetan Plateau snow. Here, we establish a snow indicator for Tibetan Plateau snow variability: the snow cover extent increment within late autumn. This snow increment indicator improves the standard deviation by 72.6% and diabatic cooling by 89.7% over the entire Tibetan Plateau, which shows a robust link to the subsequent spring Arctic sea-ice concentration. Faster Tibetan Plateau snow cover extent increment leads to stronger Tibetan Plateau cooling and disturbance along the subtropical westerly jet, thereby inducing a Tibetan Plateau-Arctic wave train and a spring Arctic cyclonic anomaly. This cyclonic system favors the reduction in spring Arctic sea-ice by equatorward sea ice drift, implying a link between spring Arctic sea-ice and the Tibetan Plateau snow increment indicator through the wave train and sea-ice dynamic processes.

npj Climate and Atmospheric Science (2023)6:191 ; https://doi.org/10.1038/s41612-023-00505-0

INTRODUCTION

Arctic sea-ice anomalies have been recognized as an indicator of local and remote climate extremes because they directly impact on the atmosphere through thermodynamic and radiative processes[1–3]. In recent decades, the Arctic has witnessed significant sea-ice loss[4–6]. The physical processes involved in Arctic sea-ice loss include oceanic warming, lapse rate feedback, Planck, albedo feedbacks, atmospheric moisture and energy transport[7–9], some of which may exacerbate Arctic warming and sea-ice melting via increased surface heating[10–12].

Arctic sea-ice variability is influenced by tropical[13–16] and mid- to high-latitude ocean-atmospheric processes[17–20] and global warming[10,21,22]. Tropical air-sea interactions, e.g., the El Niño-Southern Oscillation (ENSO) and the associated Pacific North American teleconnection, can impact summer and autumn Arctic sea-ice variability through atmospheric moisture and heat transports[13,14]. Arctic atmospheric anomalies, such as Ural blocking and variations in the polar vortex, exert prominent impacts on winter Arctic sea ice through changes in downward longwave radiation caused by water vapor, temperature changes and sea-ice drift[17,18,20]. These studies have focused mainly on summer, autumn and winter Arctic sea ice variability, but relatively few studies have examined the origin of spring Arctic sea-ice variability. Moreover, the Arctic sea-ice spring predictability barrier[23] signifies the importance of exploring the precursors of spring Arctic sea ice variability.

Previous studies suggest that preceding Tibetan Plateau (TP) snow cover anomalies could be one of the precursors to extratropical circulation systems[24–26]. This is largely because the TP snow cover has cross-seasonal climate impacts[27–33]. For instance, late autumn TP snow cover anomalies may lead to a remote winter Pacific North American teleconnection response through a persistent snow forcing from autumn to winter[24,25]. The spring TP snow cover could influence the simultaneous Aleutian Low[26]. Given that the variations in the Pacific North American teleconnection and Aleutian Low might play a role in Arctic sea-ice variability[12,13], Arctic sea-ice variability may be linked to TP snow conditions via atmospheric circulation systems. However, it is unclear whether there is a physical pathway through which the TP snow conditions can influence Arctic sea ice variability. This study aims to establish a linkage between the preceding TP snow cover and spring Arctic sea-ice variability.

A recent study[34] notes that the persistence of October-November-December (OND, late autumn) TP snow cover extent (SCE) anomalies is typically limited to within two months. This finding suggests that the OND averaged TP SCE is not a good indicator of the TP snow climate effect, especially for the impact during the ensuing seasons. To address this issue, we examine the TP SCE increment within the OND, which can improve the standard deviation by 72.6% and diabatic cooling by 89.7% over the entire Tibetan Plateau domain. The snow increment indicator can not only reflect the features in the traditional snow indicator (e.g., the degree of snow cover), but also exhibits some extra characteristics (e.g., the velocity of snow cover accumulation). In addition, the snow increment indicator associated snow anomalies can persist into the following early spring and thus establish a physical linkage with the following early spring Arctic sea-ice concentration (SIC) through sea-ice dynamic processes.

RESULTS

A snow increment indicator for the TP snow's climate impact

The TP SCE is typically approximately 34% in late winter (January to March), which varies little among these months (Table 1). The later winter SCE is mainly determined by a rapid accumulation in the TP SCE, from NOAA dataset, from 12.0% in October to 27.3% in December. That is, the seasonal increase in SCE within the OND governs the winter TP snow cover variability. Thus, to better reflect

[1]State Key Laboratory of Marine Environmental Science, College of Ocean and Earth Sciences, Xiamen University, Xiamen, China. [2]Key Laboratory of Geoscience Big Data and Deep Resource of Zhejiang Province, School of Earth Sciences, Zhejiang University, Hangzhou, China. [3]Center for Monsoon System Research, Institute of Atmospheric Physics, Chinese Academy of Sciences, Beijing, China. [4]State Key Laboratory of Numerical Modeling for Atmospheric Sciences and Geophysical Fluid Dynamics (LASG), Institute of Atmospheric Physics, Chinese Academy of Sciences, Beijing, China. [5]University of Chinese Academy of Sciences, Beijing, China. ✉email: amduan@xmu.edu.cn

Table 1. Monthly evolution of TP snow cover extent.

	Jan	Feb	Mar	Apr	May	Jun	Jul	Aug	Sep	Oct	Nov	Dec
NOAA	35.3	34.5	31.2	25.4	18.5	12.2	6.7	3.6	4.0	12.0	22.2	27.3
NSIDC	34.4	32.3	27.7	22.5	16.2	10.8	5.8	3.6	4.8	14.5	22.2	27.5

Monthly climatology of Tibetan Plateau SCE (Unit: %) based on the two SCE datasets for 1979–2021.

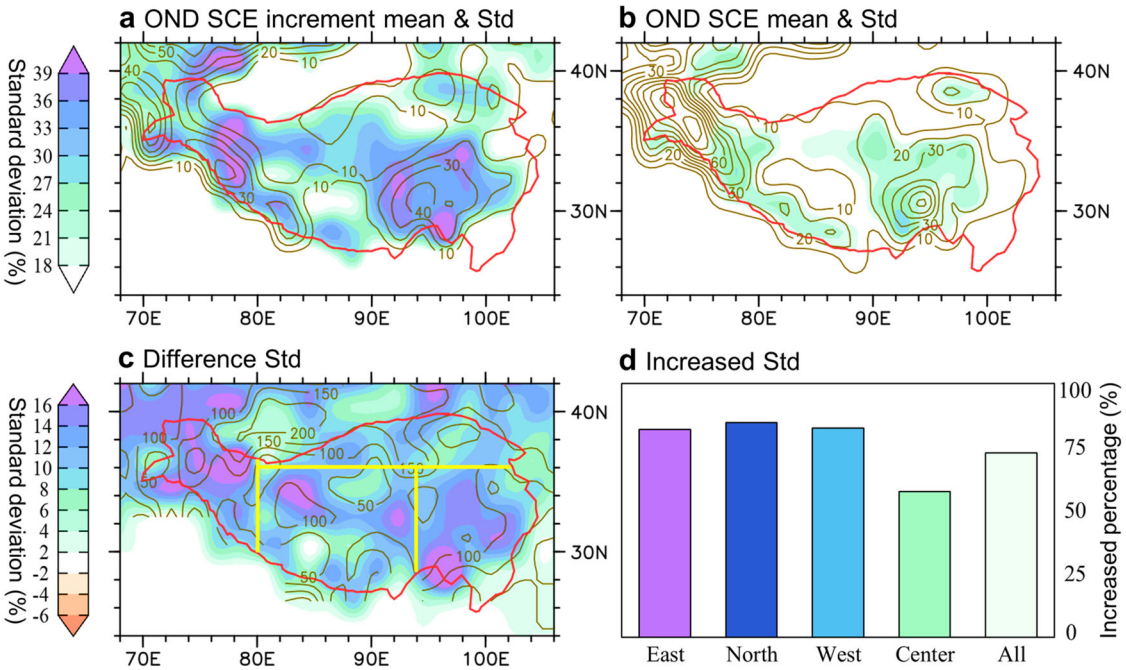

Fig. 1 Differences in the OND TP SCE increment and SCE. Contours in **a** show the 1979–2021 mean October-to-December increment in snow cover extent (SCE) over the TP, and shadings show the interannual component of the SCE increment's standard deviation. **b** Same as in **a**, but for the SCE. **c** Difference in the standard deviation shown in **a** and **b** (i.e., **a**–**b**, shadings) and the percentage increase in the standard deviation (i.e., (**a**–**b**)/**b** × 100, contours). **d** Area-weighted average of the percentage increase in the standard deviation shown by the contours in **c** over the eastern, northern, western, center, and entire TP domains. Unit is %. The red contours refer to the TP outline. The yellow lines in **c** are used to subdivide the TP into four regions. The NOAA datasets are utilized here.

this TP snow cover variability, we calculated the TP SCE increment within the OND as the difference between the December and October SCE.

Although the climatological TP SCE increment within the OND is lower than that of the OND TP SCE, the standard deviation of the interannual variations in the TP SCE increment within the OND is much larger than that in the OND SCE over the entire TP, especially over the western TP, where the maximum climatological SCE is located (Fig. 1a, b). Compared with the interannual standard deviation of the SCE, the interannual standard deviation of the SCE increment, from NOAA dataset, is enhanced by 81.8%, 84.7%, 82.4%, 57.4% and 72.6% over the eastern, northern, western, central, and entire TP, respectively (Fig. 1d and Supplementary Fig. 1). Note that the maximum SCE occurs in JFM, but the climatological SCE increment is weak, with extreme regions that are mismatched with the standard deviation. Therefore, we adopt the OND SCE increment as the possible snow indicator on the TP.

The distinct change in the interannual variabilities suggests that the TP SCE increment may be a different indicator for the TP snow's climatic impact. To examine their differences on an interannual timescale, we first construct the late autumn SCE increment index (SCEII) as the area-weighted mean of the TP SCE increment within the OND via a high-pass filter (Supplementary Fig. 2). In comparison, the late autumn interannual component of the SCE index (SCEI) is calculated based on the OND TP SCE (Supplementary Fig. 2b). The correlation of SCEII and SCEI, from NOAA dataset, is 0.49, passing the statistical significace at the 1% level. This finding indicates that the SCEII and SCEI have similar interannual variability, i.e., the faster the SCE increment is, the larger the SCE is. In addition, we chose the extreme snow years according to the SCEII and SCEI, both of which are 14 years based on the indices' absolute value exceeding 1. However, only 4 years are in the same phase among these extreme years (marked by dots in Supplementary Fig. 2b). This finding also implies that the nature of the SCEII is not totally in accordance with the SCEI because the SCEII represents the variation in the snow accumulated speed.

The SCEII well represents the SCE increment anomalies over the whole TP region (Fig. 2a), while the SCEI-related SCE anomalies are confined to the central TP area (Fig. 2b). Similar spatial distributions can be seen in the corresponding surface air temperature (SAT) fields (Fig. 2c, d). Significantly colder SAT increment anomalies over the whole TP are associated with a positive SCEII, featuring the cooling effect of surface snow cover over the entire TP. These results illustrate that the faster the TP SCE accumulated, the colder the atmosphere there. In contrast, the regression of SAT onto SCEI fails to represent the cooling

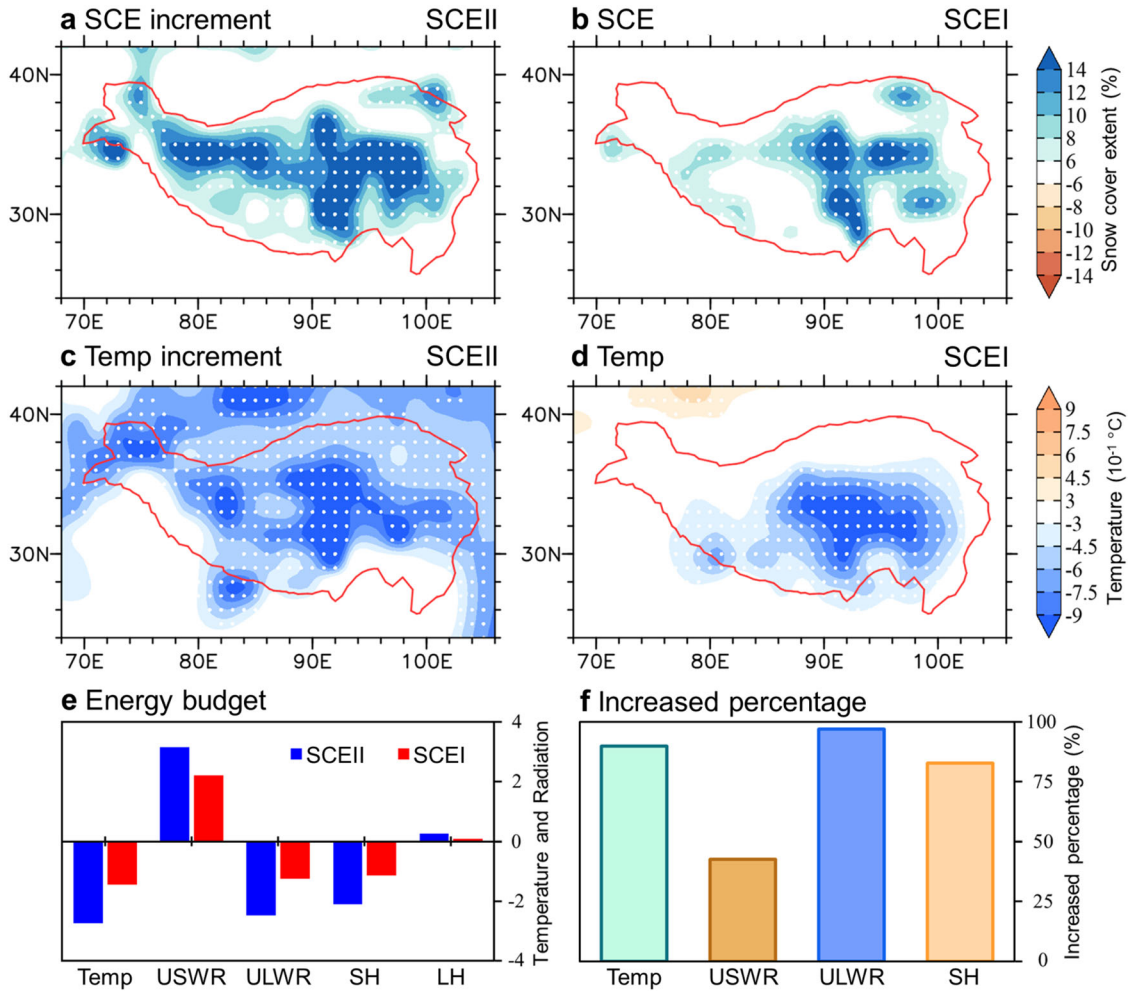

Fig. 2 Different diabatic cooling and energy budgets associated with variations in TP SCE increment and TP SCE. Anomalies of OND **a** SCE increment (unit: %) and **c** 2 m air temperature increment (unit: 10^{-1} °C) obtained by linear regression onto the SCEII during 1979–2021. **b**, **d** same as in **a**, **c** but for the SCE and 2 m air temperature regressed onto the SCEI. **e** The red and blue bars are same as in **b** and **a**, respectively, but for the TP area-weighted mean of the 2 m air temperature (unit: 10^{-1} °C), USWR, ULWR, SH and LH anomalies (red bars; unit: W m^{-2}), and its increment anomalies (blue bars). **f** Relative changes in regression coefficients in the increment field compared to that in the original field (unit: %). The stippling denotes the regions where the regression coefficients are statistically significant at the 5% level.

effect of snow cover in the western TP, where the maximum snow cover extent is located (contours in Fig. 1b).

To understand the atmospheric cooling pathways, the snow related surface energy fluxes are shown in Supplementary Fig. 3. The spatial patterns of upward shortwave radiation (USWR) increment, upward longwave radiation (ULWR) increment and surface sensible heat (SH) flux increment are closely tied to SCEII (Supplementary Fig. 3a–d), and the radiation flux anomalies are bound up with SCEI (Supplementary Fig. 3e–h), which show similar distributions to that of the SCE increment (Fig. 2c) and SCE anomalies (Fig. 2d), respectively. Moreover, both SCEII-associated latent heat (LH) flux increments and SCEI-associated LH fluxes show weak values (Supplementary Fig. 3d–h), implying that the OND snow-hydrology effect exerts a negligible role, which is consistent with a recent study[30].

The SCEII and SCEI-associated energy budgets averaged over the TP are depicted in Fig. 2e. Corresponding to the positive SCEII anomalies (i.e., faster snow accumulation in OND), the TP atmosphere tends to induce a quicker cooling effect (i.e., negative air temperature increment). The major influence is the excessive reflected solar radiation due to the fast-increasing albedo (i.e., the positive USWR increment). The excessive solar reflection leads to the cooling surface, thereby favoring the decrease in ULWR (i.e., negative ULWR increment). Additionally, faster snow accumulation reduces the SH flux increment via isolation of the land-air energy exchange. Thus, the quicker enhanced albedo and insulation effect of snow cover contribute largely to the quicker diabatic cooling.

Note that the promotion of varying degrees for the increment of diabatic cooling and radiation fluxes associated with SCEII, from NOAA dataset, appear over the TP. The quantitative analysis results show that the increments in air temperature, USWR, ULWR, and SH promotion percentages reach 89.7%, 42.5%, 96.8%, and 82.6%, respectively (Fig. 2f).

Associated with a faster SCE increase, the TP witnesses a significant negative height increment anomaly that broadly extends to much of East Asia regions (Supplementary Fig. 4a, c), while prominent negative geopotential height anomalies related to the SCEI prevail east of the TP (Supplementary Fig. 4b, d), which implies a robust circulation relationship with the TP SCE increment but a weak relationship with the TP SCE.

In summary, compared with the SCEI, the SCEII depicts a larger interannual variability, stronger diabatic cooling effect, faster snow-albedo feedback processes, and TP local atmospheric circulation linkage.

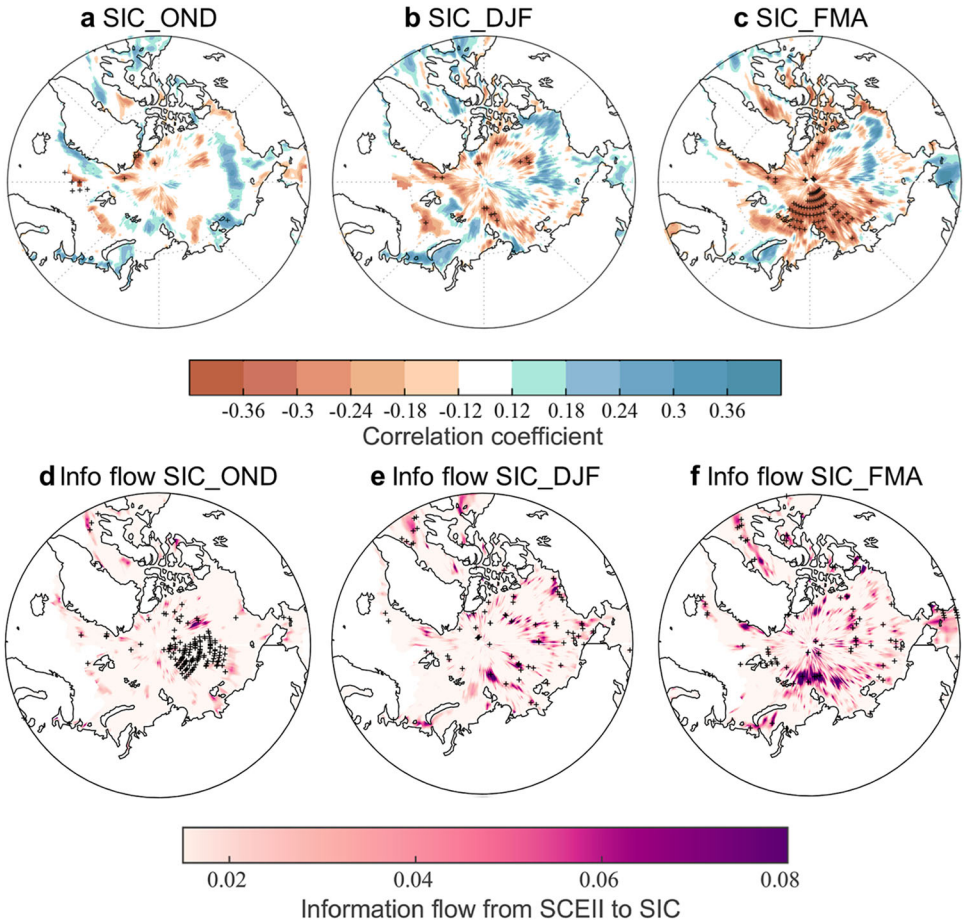

Fig. 3 Arctic SIC anomalies linked to SCEII variations. Spatial distribution of lagged correlation coefficients between SCEII and Arctic SIC during 1979–2021 in **a** OND, **b** DJF and **c** FMA. Information flow (unit: nats) from SCEII to Arctic SIC in **d** OND, **e** DJF and **f** FMA. The stippled regions denote the statistical significance at the 5% level.

Lagged relationship between the TP SCE increment and Arctic SIC

Hereafter, we utilize the OND TP SCE increment index to explore the following anomalous atmospheric circulation in the Northern Hemisphere and therefore the Arctic sea ice response to the cooling effect of TP snow cover. First, we examined the persistence of the TP snow cover (Supplementary Fig. 5). The positive TP SCE anomalies associated with the OND TP SCEII can be prolonged to the ensuing winter (December-January-February, DJF) and the early spring (February-March-April, FMA) of the next year. The persistent TP SCE anomalies favor stable impacts on the subsequent epochs[29,31,35,36]. As such, the long memory of SCEII-associated SCE anomalies provides a foundation to establish a physical linkage with the cross-seasonal climate anomalies in the FMA of the next year.

The simultaneous OND SIC anomalies associated with the SCEII are nonsignificant in the Arctic region (Fig. 3a). However, in the following DJF, the SCEII-related negative Arctic SIC anomalies begin to strengthen (Fig. 3b). In the FMA of the next year, significant negative SIC anomalies span the northern Barents Sea, northern Kara Sea, and Laptev Sea and extend to the Arctic center (Fig. 3c). The extreme SCE increment events, from the NOAA dataset, are defined based on the SCEII with the threshold of 0.9 (−0.9) standard deviation, with which a total of 11 faster and 9 slower TP SCE increment years were identified during the past 43 late autumns. Composite results are highly similar to those of the correlation panels. In addition, information flow from SCEII to Arctic SIC is weak during the OND and DJF (Fig. 3d, e), which shows large values with significant signals sweeping over the northern Barents Sea, northern Kara Sea, and Laptev Sea and extending to the Arctic center (Fig. 3f), indicating that the signals can be transmitted from the SCEII to Arctic SIC. These results further support the causal relationship of SCEII-Arctic SIC.

The extreme SCE increment events, from the NOAA dataset, after removing ENSO signals are selected when the SCEII is greater (smaller) than 0.9 (−0.9) while Niño 3.4 is smaller (greater) than 0.9 (−0.9). A total of 9 positive and 7 negative SCE increment years after removing ENSO were selected during the past 43 late autumns. After removing ENSO signals, the SCEII-related Arctic SIC patterns for both the composite (Fig. 6d–f) and partial correlation (Supplementary Fig. 6a–c) show high similarity with the results without removing ENSO signals (Fig. 3), indicating that the SCEII-SIC relationship is independent of ENSO. Therefore, theses robust statistical connection and casual analysis imply that the reduced (enhanced) Arctic SIC in the FMA may be followed by a greater (less) TP SCE increment in the preceding OND.

Potential mechanisms for the SCEII-SIC relationship

Large-scale teleconnection wave trains provide a clue to examine remote climate impacts[35,37–39]. The formation of the atmospheric wave train, especially the hemispheric scale wave train, tends to depend on the waveguide, e.g., westerly jet[31,40]. Clearly, the subtropical westerly jet (SWJ) spans North Africa, the TP, and the North Pacific Ocean and extends to the North Atlantic sector

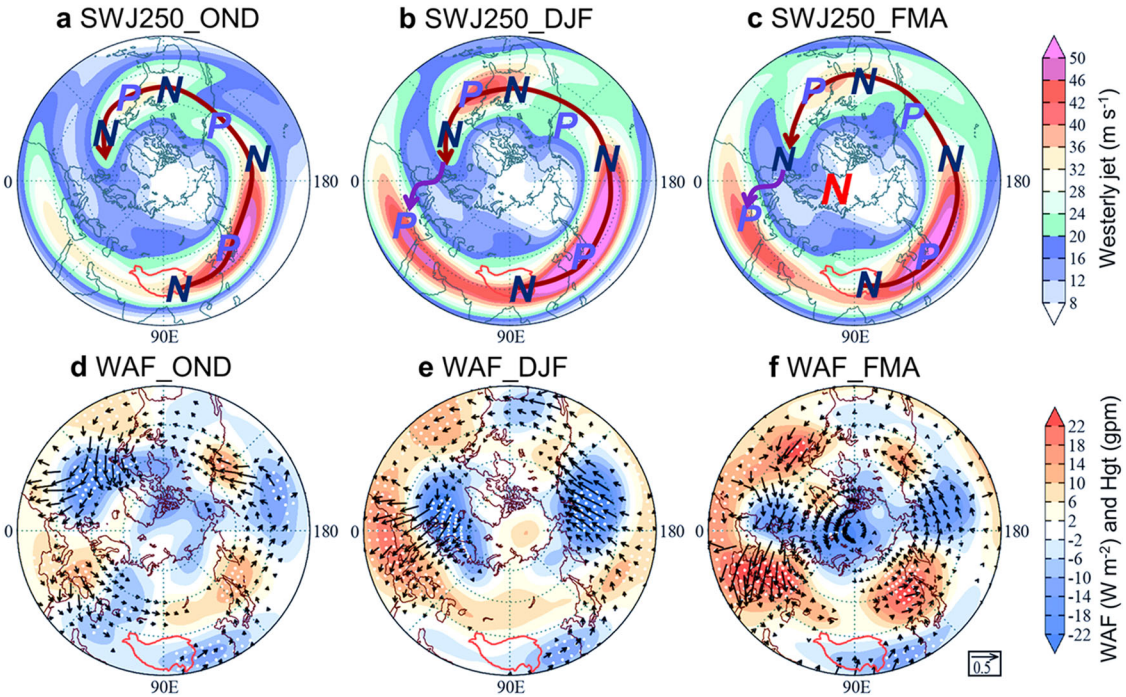

Fig. 4 The seasonal evolution of the subtropical westerly jet and SCEII-associated wave train. Spatial distribution of the climatological zonal wind (unit: m s^{-1}) at 250 hPa during **a** OND, **b** DJF, and **c** FMA. Lagged regression of 250-hPa geopotential height (shading; unit: gpm) and wave activity flux (vectors; unit: m^2 s^{-2}) during **d** OND, **e** DJF and **f** FMA with respect to SCEII. The stippled regions indicate that the geopotential height anomalies are statistically significant at the 5% level. The signs "*P*" and "*N*" in **a**–**c** refer to the positive and negative geopotential height regions in **d**–**f**, respectively. The thick arrows approximately represent the propagation of the wave train.

(Fig. 4a–c). This finding means that the SWJ may be an atmospheric waveguide that links the TP-Arctic.

To obtain insight into their connection, the SCEII-associated upper tropospheric geopotential height and wave activity flux are calculated (Fig. 4d–f). The SCEII-related local negative geopotential height anomalies prevail over the TP and extend to its east during the OND and persist to the following FMA, corresponding to the diabatic cooling associated with TP snow increment. Moreover, an anomalous wave train pattern lies along the SWJ, which is accompanied by eastward propagation of the wave activity flux from the TP, crossing the North Pacific and North Atlantic sectors, featuring a low-pressure anomaly extending to the Arctic. Therefore, the SWJ could serve as an air bridge in the SCEII-associated TP-Arctic atmospheric wave train via the jet waveguide effect. However, after removing the TP SCE variability in DJF and FMA, the SCEII-associated atmospheric wave train and its significance decreased during these epochs. These results illustrate that the SCEII-associated persistent SCE anomalies from OND to the following FMA play a crucial role in the maintenance of the atmospheric wave train (Supplementary Fig. 5 and Fig. 4d–f).

Previous studies have proposed that greater TP snow can impact large-scale atmospheric circulation through the snow albedo effect[24,26,27,36,40,41]. Here, we hypothesize that the TP SCE increment could impact the overlying atmosphere by an anomalous albedo effect. To verify this viewpoint, we designed two numerical experiments by utilizing the Community Earth System Model (CESM1.1.1), developed by the National Center for Atmospheric Research (NCAR). The control experiment was performed with the climatological sea surface temperature in 1981–2010. The perturbation experiment is the same as the control but driven by a higher TP surface albedo forcing from October to the next April (see details in Methods). The difference between the perturbation and control runs can be regarded as the response to the snow albedo forcing on the TP.

The modeled response of a negative geopotential height to the TP albedo forcing can be found over the TP (Fig. 5). In addition, the wave train pattern appears over the TP, North Pacific, and North Atlantic sectors, which are similar to the observations, especially in the following spring (Fig. 4d–f). These results further confirm that the TP SCEII can capture the TP's snow-albedo effect well, which leads to the TP-Arctic wave train.

Specifically, the negative geopotential height anomalies therein indicate that the wave train dominates the North Atlantic in the OND (Fig. 4d). Afterward, this negative geopotential height moves northward in DJF (Fig. 4e) and extends into the Arctic in FMA of the next year (Fig. 4f), which is generally reproduced in the model simulation (Fig. 5). To further investigate whether the SCEII-associated circulation anomalies could modulate the Arctic SIC, we examine the SCEII-associated thermal (Supplementary Fig. 7) and dynamic processes (Fig. 6) that are related to Arctic sea ice anomalies in the FMA. The significant low-level negative pressure anomalies and cyclonic pattern associated with SCEII occupy the northern Barents Sea, northern Kara Sea, and Laptev Sea and even extend to the central Arctic (Fig. 6a and Supplementary Fig. 7a), consistent with the upper tropospheric circulation anomalies (Fig. 4f), thus featuring a barotropic structure in the vertical direction. In contrast, the anomalous water vapor transport, specific humidity, and air temperature associated with SCEII are nonsignificant over the whole Arctic domain (Supplementary Fig. 7b, c), indicating that SCEII-associated thermal processes play a secondary role in the formation of the FMA Arctic SIC anomalies.

The SCEII-related cyclonic anomalies (purple vector, marked with blue "C" in Fig. 6a) are in accordance with its climatological wind direction (green vector as shown in Fig. 6a), thereby intensifying the cyclonic wind stress anomalies (Fig. 6b).

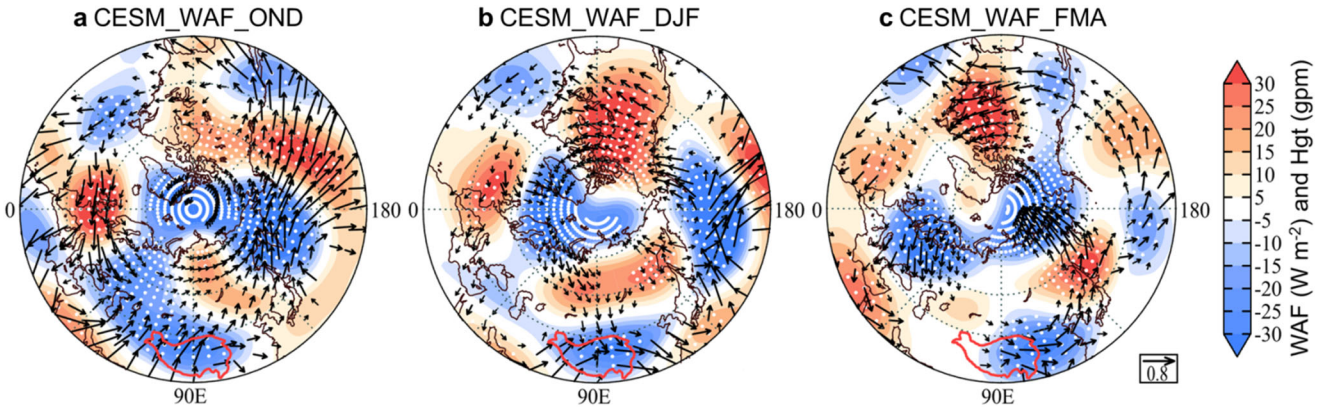

Fig. 5 Atmospheric circulation response in the CESM simulation. Response of **a** OND, **b** DJF and **c** FMA wave activity flux (vectors; unit: W m^{-2}) and geopotential height (shadings; unit: gpm) anomalies at 250-hPa to the TP albedo forcing obtained by the difference response between the high albedo and control experiments. The stippled regions indicate the statistical significance of the geopotential height anomalies at the 5% level.

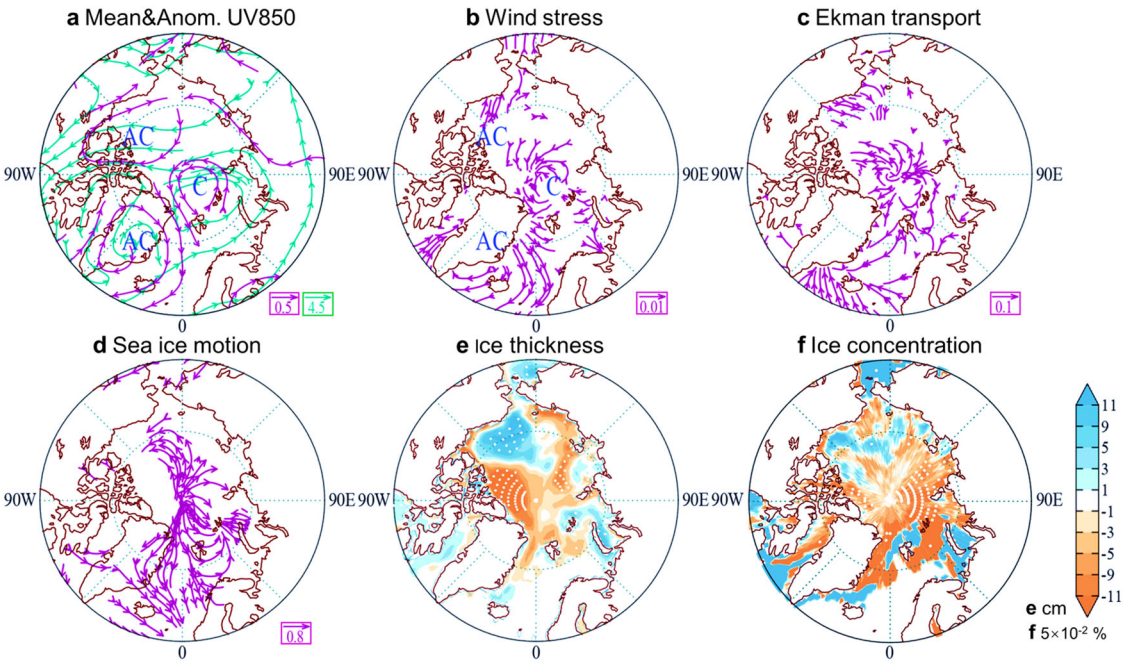

Fig. 6 Dynamical processes associated with SCEII. Anomalous FMA **a** 850-hPa wind (purple vectors; unit: m s^{-1}), **b** wind stress (unit: N m^{-2}), **c** Ekman transport (unit: m^2 s^{-1}), **c** sea ice drift (unit: cm s^{-1}), **e** sea ice thickness (unit: cm) and **f** SIC (unit: 5×10^{-2} %) derived from regression onto SCEII. Green vectors in **a** show the climatological FMA wind (unit: m s^{-1}) at 850 hPa. The stippled regions and purple vectors indicate the statistical significance of the regression coefficients at the 5% level. The signs "AC" and "C" in **a** and **b** refer to the anticyclone and cyclone anomalies, respectively.

According to the relationship between the wind stress and Ekman transport, the Northern Hemispheric Ekman transport is directed to the right of the wind stress. Therefore, the anomalous Ekman transport (Fig. 6c) associated with SCEII favors sea-ice drift that leaves the Arctic center and moves to the North Atlantic (Fig. 6d). Moreover, the anomalous outward ice drift of the Arctic sea-ice leads to a pronounced reduction in the Arctic sea ice thickness and SIC (Fig. 6e, f). In summary, the OND TP SCE increment could impact the subsequent FMA Arctic SIC variability via the dynamic pathway.

DISCUSSION

The formation and maintenance of the hemispheric-scale wave train. Previous studies proposed that the Rossby wave source (RWS) could be used to investigate the formation of a large-scale wave train[31,42,43]. As mentioned above, the SCEII-associated hemispheric-scale atmospheric wave train sweeps along the SWJ. To examine the formation of this wave train anomaly, the SCEII-associated RWS anomalies are calculated (Supplementary Fig. 8). The SCEII-associated significant divergence anomalies in the upper troposphere prevail over the TP due to the positive snowfall and moisture convergence anomalies (Supplementary Fig. 9), which favor the negative RWS and disturbance anomalies over the TP (Supplementary Fig. 8). Moreover, RWS anomalies along the SWJ contribute to the formation of the hemispheric wave train with the aid of the SWJ waveguide.

Regarding the maintenance of the wave train anomaly, both SCEII-associated barotropic energy conversion from the background flow (Supplementary Fig. 10a–c) and transient eddy activity

via wave-flow interaction (Supplementary Fig. 10g–i) make major contributions. In contrast, the baroclinic energy conversion lies over the TP and extends to its east (Supplementary Fig. 10d–f), which illustrates that the snow-atmosphere interaction could be maintained through baroclinic energy feedback over these regions.

The development of the negative geopotential height in the North Atlantic. The SCEII-associated negative geopotential height anomalies over the North Atlantic, which move northward and extend to the Arctic region, are the key system influencing the FMA SIC anomaly (Fig. 4d–f). The northward-extending low anomalies are also observed from the vertical cross-section panels (Supplementary Fig. 11a). The SCEII-associated negative geopotential height anomalies appear in the troposphere in OND, followed by northward movement and reaching the stratosphere in the subsequent January and February, finally forming a deep barotropic structure throughout the Arctic stratosphere and troposphere in the March (Supplementary Fig. 11a). The tropospheric and stratospheric evolution of the geopotential height anomalies from the North Atlantic to the Arctic could be demonstrated with the Eliassen Palm (EP) flux[6,39]. The EP flux anomalies show clear upward propagation from January to February and downward propagation in March, explaining the evolution of geopotential height anomalies associated with SCEII (Supplementary Fig. 11b). Consequently, the northward propagation of the negative geopotential height anomalies is mainly due to the tropospheric and stratospheric coupling processes.

In summary, this study suggests that the OND TP SCE increment could be a better indicator of the late autumn TP snow climatic effect in terms of local atmospheric responses and remote Arctic sea ice linkage on the interannual time scale (Supplementary Fig. 12). Note that the FMA SIC differences lie in the weak correlation (Fig. 3c) and the apparent regression (Fig. 6f) east of Greenland, which are probably because the SCEII-associated pronounced sea ice drift anomalies decrease the SIC, while the SCEII-associated cold air anomalies increase the SIC. Therefore, the SIC-related thermal process weakens the significant dynamical process, resulting in a reduction in the significance of SIC in east of Greenland.

We also examine the trend of the OND TP SCE increment, which features a weak trend. This finding indicates that the snow increment indicator exerts a limited role in the sharply reduced Arctic SIC in recent decades, whereas the sharply decreased Arctic SIC is largely due to greenhouse gas-induced global warming[11].

Note that a high correlation (i.e., 0.89) occurs between the original SCEII (without filter) and the SCEII (Supplementary Fig. 2a). We further depicted the original SCEII-associated Arctic SIC anomalies (Supplementary Fig. 13). Clearly, the original SCEII-associated SIC anomalies (Supplementary Fig. 13c) show high similarity with the SCEII-related SIC pattern in FMA (Fig. 3c), while the SIC patterns are not in accordance during OND and DJF, implying differences in the SCEII with and without filtering.

In addition, given that the tropical Indian and North Atlantic Oceans sea surface temperature (SST) plays an important role in the Arctic SIC anomalies, we further investigate the SCEII-SIC relationship after removing SST signals there in FMA (Supplementary Fig. 14). When the SST signals are excluded, the SCEII-associated SIC anomalies (Supplementary Fig. 14a, b) show high similarity with the original pattern (Fig. 3c). The SCEII-associated wave fluxes travel to the Arctic and the Arctic negative height anomalies therein, suggesting that the TP SCE increment could be independent of those SST signals to impact the Arctic SIC anomalies by the atmospheric wave train (Supplementary Fig. 14c, d). Note that the atmospheric wave train after removing tropical Indian Ocean SST signals (Supplementary Fig. 14c) shows some differences from the original (Fig. 4f), e.g., with the former featuring a northward transport pathway. These differences require further investigation in future work.

METHODS

Observational and reanalysis datasets

The time range of the analysis in this study is 1979–2021: (i) The Northern Hemisphere weekly snow cover extent (SCE) records on 25 km × 25 km grids were obtained from the National Snow and Ice Data Center (NSIDC)[44]. (ii) The other weekly SCE records were extracted from the National Oceanic and Atmospheric Administration (NOAA) Climate Data Record (CDR)[45]. Both the NSIDC and NOAA weekly SCE datasets were based on multiple satellite and sensor retrievals. (iii) The daily snow depth product was obtained from the Big Earth Data Platform for Three Poles[46]. These data are based on a passive microwave remote-sensing method. The original products have been converted into the monthly snow depth on 0.25° grids. (iv) The monthly snowfall data on 0.25° grids were obtained from the European Center for Medium-Range Weather Forecast's fifth generation reanalysis (ERA5)[47]. (v) Polar pathfinder daily sea-ice motion vector data (latest version 4) were obtained from NSIDC[48], which are on 25 km × 25 km grids and derived from multiple sensors, e.g., the advanced very high resolution radiometer (AVHRR), advanced microwave scanning radiometer (AMSR), scanning multichannel microwave radiometer (SMMR) and special sensor microwave imagers (SSM/I). (vi) Monthly data on 0.25° grids for surface wind stress, Ekman transport, sea-ice thickness and sea-ice concentration were obtained from the fifth generation of ECMWF's ocean reanalysis system (OCEAN5) and its real-time analysis component (ORAS5)[49]. (vii) Monthly mean sea ice concentration and sea surface temperature data on 1° grids were obtained from the Hadley Center Sea Ice and Sea Surface Temperature dataset (HadISST)[50]. (viii) The daily and monthly data for atmospheric circulation fields (i.e., winds, geopotential height, and specific humidity) on 2.5° grids and surface energy fluxes (i.e., shortwave radiation, and sensible heat) on T62 Gaussian girds were obtained from the National Centers for Environmental Prediction–Department of Energy (NCEP–DOE) Reanalysis-2[51].

Dynamic diagnosis of the TP-Arctic atmospheric wave train

The wave activity flux is employed to determine the atmospheric wave propagation, which indicates the propagation of the quasi-stationary Rossby wave train[52]. In the pressure coordinate, the horizontal wave activity flux is written as follows:

$$W = \frac{1}{2|\mathbf{U}|}\begin{pmatrix} U(\varphi_x'^2 - \varphi'\varphi_{xx}') + V(\varphi_x'\varphi_y' - \varphi'\varphi_{xy}') \\ U(\varphi_x'\varphi_y' - \varphi'\varphi_{xy}') + V(\varphi_y'^2 - \varphi'\varphi_{yy}') \end{pmatrix} \quad (1)$$

where $\mathbf{U} = (U, V)$ refers to the zonal and meridional components of the geostrophic winds. p and φ represent the normalized pressure and three-dimensional stream function, respectively. The symbols of primes and subscripts denote the deviations from the time mean and the partial derivatives, respectively.

The Rossby wave source (RWS) is calculated to examine the formation of atmospheric waves[53]. The RWS is written as follows:

$$S = -\nabla_H \cdot \left[\boldsymbol{u}_\chi'\left(f + \overline{\zeta}\right)\right] - \nabla_H \cdot \left[\overline{\boldsymbol{u}}_\chi \zeta'\right] \quad (2)$$

where $\boldsymbol{u}_\chi = (u_\chi, v_\chi)$. $\boldsymbol{u}_\chi = (u_\chi, v_\chi)$. u_χ and v_χ refer to the longitudinal and latitudinal components of the divergent wind, respectively. ∇_H, ζ, and $f + \zeta$ represent the horizontal gradient, relative vorticity, and absolute vorticity, respectively.

Energy conversion can be used to estimate the maintenance of large-scale atmospheric waves by extracting energy from the basic flow through the baroclinic and barotropic conversion pathways[54,55]. The baroclinic and barotropic energy conversion are

decomposed as

$$CP = -\frac{f}{\sigma}(v'T'\frac{\partial \overline{u}}{\partial p} + u'T'\frac{\partial \overline{v}}{\partial p}) \quad (3)$$

$$CK = \frac{v'^2 - u'^2}{2}\left(\frac{\partial \overline{u}}{\partial x} - \frac{\partial \overline{v}}{\partial y}\right) - u'v'(\frac{\partial \overline{u}}{\partial y} + \frac{\partial \overline{v}}{\partial x}) \quad (4)$$

$$\sigma = \frac{R\overline{T}}{C_p p} - \frac{d\overline{T}}{dp} \quad (5)$$

where R, f, and C_p denote the gas constant tied to dry air, Coriolis force parameter, and specific heat at constant pressure, respectively.

The Eliassen Palm (EP) flux can be used to reflect the meridional propagation of the quasi-stationary planetary wave[56,57]. The EP flux (denoted $\boldsymbol{F}$) and its corresponding divergence (denoted Div) are given as follows:

$$\boldsymbol{F}=(F(\varphi),F(p)) = \left(-\rho r\cos\varphi\overline{v'u'}, \rho r f\cos\varphi\frac{\overline{v'\theta'}}{\overline{\theta_p}}\right) \quad (6)$$

$$Div = \frac{\nabla \cdot F}{\rho r\cos\varphi} \quad (7)$$

where, ρ, r, φ and f denote the standard air density, the radius of the earth, the latitude, and the Coriolis parameter, respectively. $\nabla \cdot F$ refers to the divergence of EP flux. θ and ρ refer to the potential temperature and standard air density, respectively. $F(\varphi)$ and $F(p)$ refer to the meridional and vertical components of the EP flux, respectively. $\overline{v'u'}$ and $\overline{v'\theta'}$ indicate the momentum disturbance transport in the meridional direction and sensible heat flux, respectively. The symbols with primes and overbars, in formulas 2–6, are the anomalies of variables and their climatology, respectively.

Causal analysis

To determine causation, the information flow method is used based on information theory and first principles[58,59]. The information flow from x_2 to x_1 per unit time is determined according to Liang–Kleeman information flow theory[58], which is expressed as[59]

$$\hat{T}_{2\to1} = \frac{C_{11}C_{12}C_{2,d1} - C_{12}^2C_{1,d1}}{C_{11}^2C_{22} - C_{11}C_{12}^2} \quad (8)$$

$$C_{ij} = \overline{(x_i - \overline{x_i})(x_j - \overline{x_j})} \quad (9)$$

$$\dot{x}_{j,n} = (x_{j,n+k} - x_{j,n})/k\triangle t \quad (10)$$

where C_{ij} refers to the covariance matrix between timeseries x_1 and x_2. $C_{i,dj}$ denotes the covariance between x_i and the Euler forward differencing scheme of formula (10). Δt refers to the time step. According to this theory, if $T_{2\to1} \neq 0$, x_2 causes x_1; if the information flow from x_2 to x_1 equals zero, it means no causality.

Numerical model simulation

The state-of-the-art Community Earth System Model (CESM) version 1.1.1 was used to validate the atmospheric responses to the idealized TP albedo forcing, which is a fully coupled model developed by the National Center for Atmospheric Research (NCAR). The atmospheric component model is the Community Atmospheric Model of version 5.0 (CAM5.0), which has a $2.5° \times 1.875°$ horizontal resolution and 31 levels of vertical resolution[60]. The land component model with the same resolution as CAM is the Community Land Model version 4.0 (CLM4.0)[61]. The sea ice component model is Community Ice CodE version 4.0 (CICE4.0), which has a nonuniformly spacing grid with 384×320 cells[62]. In this study, we employed the CAM5.0 component coupled with the CLM4.0 and CICE4.0 components.

Here, we designed two numerical experiments to explore the impact of TP snow increment anomalies on large-scale atmospheric circulation via the snow-albedo effect. The first one is a control experiment, in which the climatological monthly sea surface temperature in 1980–2010 is added. The second experiment is a perturbation experiment that is designed by adding 0.4 to the albedo (soil albedo of approximately 0.4–0.5) but no more than 0.85 (snow albedo of approximately 0.85) over the entire TP (76°E-103°E, 28°N-38°N) from October to the subsequent April to represent the heavier TP snow anomaly induced persistent high albedo forcing. Note that if the perturbated albedo exceeds the TP snow-albedo (approximately 0.85), the albedo is fixed at 0.85.

In both experiments, the model is integrated for 20 years. The difference in model responses in the last 19 years between the perturbation run and control run from October to the following April was utilized to reflect the high albedo forcing over the TP. Thus, the model simulation could further provide insight into the SCEII associated physical processes via the snow albedo effect.

Statistical analysis

Eight year high-pass filtering with the Gaussian filter method is employed to investigate the interannual variability. The zonal wavenumber 1–3 component is extracted to represent the quasi-stationary planetary wave activity via Fourier harmonics decomposition. The Niño 3.4 index is employed to reflect the ENSO signals. Based on the two-tailed Student's t test, anomalies of the variables with a 5% statistical significance level are plotted in the current studies.

DATA AVAILABILITY

The NOAA SCE data employed in the current study is available at https://www.ncei.noaa.gov/access/metadata/landing-page/bin/iso?id=gov.noaa.ncdc:C00756. Data for the NSIDC SCE is available at http://nsidc.org/data/NSIDC-0046/versions/4. A Big Earth Data Platform for Three Poles snow depth data is available at https://poles.tpdc.ac.cn/zh-hans/data/df40346a-0202-4ed2-bb07-b65dfcda9368/. The ERA5 snowfall data is available at https:// cds.climate.copernicus.eu/cdsapp#!/dataset/reanalysis-era5-single-levels-monthly-means?tab=form. The NSIDC sea ice motion data is available at https://nsidc.org/data/nsidc-0116/versions/4. The ORAS5 global ocean reanalysis data is available at https://cds.climate.copernicus.eu/cdsapp#!/dataset/reanalysis-oras5?tab=form. The HadISST SIC and SST data are available at https://www.metoffice.gov.uk/hadobs/hadisst/. The NCEP–DOE Reanalysis-2 data is available at http://downloads.psl.noaa.gov/Datasets/ncep.reanalysis2.derived/. The CESM simulation data is available from the corresponding author upon request.

CODE AVAILABILITY

The Fortran-language scripts used to post-process the data and the additional data to this paper are available from the corresponding author upon reasonable request. The MATLAB code for causal analysis is available at http://www.ncoads.cn/article/show/63.aspx.

Received: 20 June 2023; Accepted: 18 October 2023;
Published online: 17 November 2023

REFERENCES

1. Bailey, H. et al. Arctic sea-ice loss fuels extreme European snowfall. *Nat. Geosci.* **14**, 1–6 (2021).
2. Dai, A. & Song, M. Little influence of Arctic amplification on mid-latitude climate. *Nat. Clim. Chang.* **10**, 1–7 (2020).
3. Screen, J. et al. Consistency and discrepancy in the atmospheric response to Arctic sea-ice loss across climate models. *Nat. Geosci.* **11**, 155–163 (2018).
4. Duan, A. et al. Sea ice loss of the Barents-Kara Sea enhances the winter warming over the Tibetan Plateau. *npj Clim. Atmos. Sci.* **5**, 26 (2022).
5. Ouyang, Z. et al. Sea-ice loss amplifies summertime decadal CO2 increase in the western Arctic Ocean. *Nat. Clim. Chang.* **10**, 1–7 (2020).

6. Kim, B. M. et al. Weakening of the stratospheric polar vortex by Arctic sea-ice loss. *Nat. Commun.* **5**, 4646 (2014).
7. Pithan, F. & Mauritsen, T. Arctic amplification dominated by temperature feedbacks in contemporary climate models. *Nat. Geosci.* **7**, 181–184 (2014).
8. Jenkins, M. & Dai, A. The impact of Sea-Ice loss on Arctic climate feedbacks and their role for Arctic Amplification. *Geophys. Res. Lett.* **48**, e2021GL094599 (2021).
9. Zhang, P. et al. More frequent atmospheric rivers slow the seasonal recovery of Arctic sea ice. *Nat. Clim. Chang.* **13**, 266–273 (2023).
10. Jun, S.-Y., Ho, C.-H., Jeong, J.-H., Choi, Y.-S. & Kim, B. M. Recent changes in winter Arctic clouds and their relationships with sea ice and atmospheric conditions. *Tellus A.* **68**, 29130 (2016).
11. Screen, J. & Simmonds, I. The central role of diminishing sea ice in recent Arctic temperature amplification. *Nature* **464**, 1334–1337 (2010).
12. Dai, A., Luo, D., Song, M. & Liu, J. Arctic amplification is caused by sea-ice loss under increasing CO2. *Nat. Commun.* **10**, 121 (2019).
13. Liu, Z. Acceleration of western Arctic sea ice loss linked to the Pacific North American pattern. *Nat. Commun.* **12**, 1519 (2021).
14. Clancy, R., Bitz, C. & Blanchard-Wrigglesworth, E. The influence of ENSO on Arctic sea ice in large ensembles and observations. *J. Climate* **234**, 1–50 (2021).
15. Ding, Q. et al. Fingerprints of internal drivers of Arctic sea ice loss in observations and model simulations. *Nat. Geosci.* **12**, 28–33 (2019).
16. Topal, D., Ding, Q., Ballinger, T. & Li, Z. Discrepancies between observations and climate models of large-scale wind-driven Greenland melt influence sea-level rise projections. *Nat. Commun.* **13**, 6833 (2022).
17. Luo, B., Luo, D., Wu, L., Zhong, L. & Simmonds, I. Atmospheric circulation patterns which promote winter Arctic sea ice decline. *Environ. Res. Lett.* **12**, 1–13 (2017).
18. Zhang, J. et al. Responses of Arctic sea ice to stratospheric ozone depletion. *Sci. Bull.* **67**, 1182–1190 (2022).
19. Stone, K., Solomon, S. & Kinnison, D. Prediction of northern hemisphere regional sea ice extent and snow depth using stratospheric ozone information. *J. Geophys. Res. Atmosphere* **125**, e2019JD031770 (2020).
20. Sumata, H., de Steur, L., Divine, D., Granskog, M. & Gerland, S. Regime shift in Arctic Ocean sea ice thickness. *Nature* **615**, 443–449 (2023).
21. Ding, Q. et al. Influence of high-latitude atmospheric circulation changes on summertime Arctic sea ice. *Nat. Clim. Chang.* **7**, 289–295 (2017).
22. Kay, J., Holland, M. & Jahn, A. Inter-annual to multi-decadal Arctic sea ice extent trends in a warming world. *Geophys. Res. Lett.* **38**, L15708 (2011).
23. Bushuk, M., Winton, M., Bonan, D., Blanchard-Wrigglesworth, E. & Delworth, T. A mechanism for the Arctic Sea ice spring predictability barrier. *Geophys. Res. Lett.* **47**, e2020GL088335 (2020).
24. Liu, S. et al. Modeled northern hemisphere autumn and winter climate responses to realistic Tibetan Plateau and Mongolia snow anomalies. *J. Climate* **30**, 9435–9454 (2017).
25. Wu, Q., Hu, H. & Zhang, L. Observed influences of autumn-early winter Eurasian snow cover anomalies on the hemispheric PNA-like variability in winter. *J. Climate* **24**, 2017–2023 (2011).
26. Wang, Z., Wu, R., Duan, A. & Qu, X. Influence of eastern Tibetan Plateau spring snow cover on North American air temperature and its interdecadal change. *J. Climate* **33**, 5123–5139 (2020).
27. Li, W. et al. Influence of Tibetan Plateau snow cover on East Asian atmospheric circulation at medium-range time scales. *Nat. Commun.* **9**, 4243 (2018).
28. Zhang, C., Guo, Y. & Wen, Z. Interdecadal change in the effect of Tibetan Plateau snow cover on spring precipitation over Eastern China around the early 1990s. *Climate Dyn.* **58**, 2807–2824 (2022).
29. Jia, X., Zhang, C., Wu, R. & Qian, Q. Influence of Tibetan Plateau autumn snow cover on interannual variations in spring precipitation over southern China. *Climate Dyn.* **56**, 767–782 (2021).
30. Zhang, C. & Jia, X. The seasonal evolution of the Tibetan Plateau snow cover related moisture during spring-to-summer. *J. Geophys. Res. Atmos.* **127**, e2022JD036560 (2022).
31. Zhang, C., Jia, X. & Wen, Z. Increased impact of the Tibetan Plateau spring snow cover to the Mei-yu rainfall over the Yangtze River Valley after the 1990s. *J. Clim.* **34**, 5985–5997 (2021).
32. Kraaijenbrink, P., Stigter, E., Yao, T. & Immerzeel, W. W. Climate change decisive for Asia's snow meltwater supply. *Nat. Clim. Chang.* **11**, 1–7 (2021).
33. Smith, T. & Bookhagen, B. Changes in seasonal snow water equivalent distribution in High Mountain Asia (1987 to 2009). *Sci. Adv.* **4**, e1701550 (2018).
34. Liu, S., Wu, Q., Yao, Y., Schroeder, S. & Wang, L. Impacts of autumn-winter Tibetan Plateau snow anomalies on North Atlantic-Europe and Arctic climate. *J. Geophys. Res. Atmos.* **127**, 2021JD035791 (2022).
35. Zhang, T. et al. The weakening relationship between Eurasian spring snow cover and Indian summer monsoon rainfall. *Sci. Adv.* **5**, eaau8932 (2019).
36. Xiao, Z. & Duan, A. Impacts of Tibetan Plateau snow cover on the interannual variability of the East Asian Summer Monsoon. *J. Clim.* **229**, 8495–8514 (2016).
37. Hu, S. & Zhou, T. Skillful prediction of summer rainfall in the Tibetan Plateau on multiyear time scales. *Sci. Adv.* **7**, eabf9395 (2021).
38. Koll, R. et al. Drying of Indian subcontinent by rapid Indian Ocean warming and a weakening land-sea thermal gradient. *Nat. Commun.* **6**, 7423 (2015).
39. Hu, D., Guan, Z., Tian, W. & Ren, R. Recent strengthening of the stratospheric Arctic vortex response to warming in the central North Pacific. *Nat. Commun.* **9**, 1697 (2018).
40. Qian, Q., Jia, X. & Wu, R. Changes in the impact of the autumn Tibetan Plateau snow cover on the winter temperature over North America in the mid-1990s. *J. Geophys. Res. Atmos.* **124**, 2019JD030245 (2019).
41. Henderson, G., Peings, Y., Furtado, J. & Kushner, P. Snow–atmosphere coupling in the Northern Hemisphere. *Nat. Clim. Chang.* **8**, D3 (2018).
42. An, X. et al. Effect of rainfall-induced diabatic heating over southern China on the formation of wintertime haze on the North China Plain. *Atmos. Chem. Phys.* **22**, 725–738 (2022).
43. Hoskins, B. & Ambrizzi, T. Rossby wave propagation on a realistic longitudinally varying flow. *J. Atmos. Sci.* **50**, 1661–1671 (1993).
44. Brodzik, M. J., & Armstrong, R. Northern Hemisphere EASE-Grid 2.0 Weekly Snow Cover and Sea Ice Extent, Version 4 [NSIDC-0046]. Boulder, Colorado USA. NASA National Snow and Ice Data Center Distributed Active Archive Center http://nsidc.org/data/NSIDC-0046/versions/4 (2013). Accessed: 07-01-2022.
45. Robinson, D. A., Estilow, T. W., & Program N. C., NOAA Climate Data Record (CDR) of Northern Hemisphere (NH) Snow Cover Extent (SCE), Version 1 [NCDC: C00756]. NOAA National Centers for Environmental Information https://www.ncei.noaa.gov/access/metadata/landing-page/bin/iso?id=gov.noaa.ncdc:C00756 (2012). Accessed: 06-03-2022.
46. Tao, C., & Liyun, D. Long-term series of daily snow depth dataset in China (1979-2021). A big earth data platform for three poles http://poles.tpdc.ac.cn/zh-hans/data/df40346a-0202-4ed2-bb07-b65dfcda9368/ (2015). Accessed on 10-May-2021.
47. Hersbach, H. et al. ERA5 monthly averaged data on single levels from 1959 to present. Copernicus Climate Change Service (C3S) Climate Data Store (CDS) https://cds.climate.copernicus.eu/cdsapp#!/dataset/reanalysis-era5-single-levels-monthly-means?tab=form (2019). Accessed on 22-Apr-2021.
48. M. Tschudi, Meier, W. N., Stewart, J. S., Fowler, C., & Maslanik, J. Polar Pathfinder Daily 25 km EASE-Grid Sea Ice Motion Vectors, Version 4. [NSIDC-0116]. Boulder, Colorado USA. NASA National Snow and Ice Data Center Distributed Active Archive Center https://nsidc.org/data/nsidc-0116/versions/4 (2019). Accessed: 07-01-2022.
49. Zuo, H., Balmaseda, M. A., Mogensen, K., & Tietsche, S. OCEAN5: the ECMWF Ocean Reanalysis System and its Real-Time analysis component. ECMWF Technical Memoranda. https://cds.climate.copernicus.eu/cdsapp#!/dataset/reanalysis-oras5?tab=form (ECMWF, 2018). Accessed: 4-July-2022.
50. Rayner, N. A. et al. Global analyses of sea surface temperature, sea ice, and night marine air temperature since the late Nineteenth Century. *J. Geophys. Res.* **108**, D14 (2003).
51. Kanamitsu, M. NCEP-DOE AMIP-II reanalysis (R-2). *Bull. Am. Meteorol. Soc.* **83**, 1631–1643 (2002).
52. Takaya, K. & Nakamura, H. A formulation of a phase-independent wave-activity flux for stationary and migratory quasigeostrophic eddies on a zonally varying basic flow. *J. Atmos. Sci.* **58**, 608–627 (2001).
53. Sardeshmukh, P. & Hoskins, B. The generation of global rotational flow by steady idealized tropical divergence. *J. Atmos. Sci.* **45**, 1228–1251 (1988).
54. Hoskins, B., James, I. & White, G. The shape, propagation and mean-flow interaction of large-scale weather systems. *J. Atmos. Sci.* **40**, 1595–1612 (1983).
55. Kosaka, Y. & Nakamura, H. Structure and dynamics of the summertime Pacific-Japan (PJ) teleconnection pattern. *Q. J. R. Meteorol. Soc.* **132**, 2009–2030 (2006).
56. Edmon, H. J., Hoskins, B. J. & McIntyre, M. E. Eliassen-Palm cross sections for the troposphere. *J. Atmos. Sci.* **37**, 2600–2616 (1980).
57. Plumb, R. On the three-dimensional propagation of stationary waves. *J. Atmos. Sci.* **42**, 217–229 (1985).
58. Liang, X. S. & Kleeman, R. Information transfer between dynamical system components. *Phys. Rev. Lett.* **95**, 244101 (2005).
59. Liang, X. S. Information flow and causality as rigorous notions *ab initio*. *Phys. Rev. E.* **94**, 052201 (2016).
60. Park, S., Bretherton, C. S. & Rasch, P. J. Integrating cloud processes in the Community Atmosphere Model, Version 5. *J. Clim.* **27**, 6821–6856 (2014).
61. Lawrence, D. M. et al. The CCSM4 Land Simulation, 1850-2005: assessment of surface climate and new capabilities. *J. Clim.* **25**, 2240–2260 (2012).
62. Hunke, E., & Lipscomb, W. *CICE: The Los Alamos Sea Ice Model Documentation and Software Use's Manual Version 4.0 LA-CC-06-012*. Los Alamos National Laboratory Technical Report Technical Report, LA-CC-06-012,1–73 (2010).

ACKNOWLEDGEMENTS

We acknowledge Prof. Aiguo Dai (State University of New York, USA) and Dr. Pengfei Zhang (Pennsylvania State University, USA) for their valuable comments and revision, which were constructive in improving the paper. The authors thank Guanqi Fu for her MATLAB technical and code support. This work was funded by the National Natural Science Foundation of China (42305016, 42030602). Chao Zhang was supported by the Outstanding Postdoctoral Scholarship, State Key Laboratory of Marine Environmental Science at Xiamen University.

AUTHOR CONTRIBUTIONS

C.Z. conceived the research, data analysis, and drafted the original manuscript; C.Z. Z.W. and Z.P. designed the CESM experiments. A.D. and X.J. provided comments and revised the paper.

COMPETING INTERESTS

The authors declare no competing interests.

ADDITIONAL INFORMATION

Supplementary information The online version contains supplementary material available at https://doi.org/10.1038/s41612-023-00505-0.

Correspondence and requests for materials should be addressed to Anmin Duan.